HHS Public Access

Author manuscript

Cancer Immunol Res. Author manuscript; available in PMC 2023 January 01.

Published in final edited form as:

Cancer Immunol Res. 2022 July 01; 10(7): 800–810. doi:10.1158/2326-6066.CIR-21-1050.

Immunological features in *de novo* and recurrent glioblastoma associate with survival outcomes

Cécile Alanio[1,2,3,4,5,6,*,‡], **Zev A. Binder**[6,7,8,*], **Renee B. Chang**[6,8,9,*], **MacLean P. Nasrallah**[6,10,*], **Devora Delman**[6,8,9], **Joey H. Li**[8], **Oliver Y. Tang**[6,11], **Logan Y. Zhang**[6,7,8], **Jiasi Vicky Zhang**[6,7,8], **E. John Wherry**[3,4,5,6,+], **Donald M. O'Rourke**[6,7,8,+], **Gregory L. Beatty**[6,8,9,+,‡]

[1]INSERM U932, PSL University, Institut Curie, Paris 75005, France

[2]Laboratoire d'immunologie clinique, Institut Curie, Paris 75005, France

[3]Institute for Immunology, Perelman School of Medicine, University of Pennsylvania, Philadelphia, PA, 19104 USA

[4]Department of Systems Pharmacology and Translational Therapeutics, Perelman School of Medicine, University of Pennsylvania, Philadelphia, PA, 19104 USA

[5]Parker Institute for Cancer Immunotherapy at University of Pennsylvania, Philadelphia, PA, 19104 USA

[6]Glioblastoma Translational Center of Excellence, Abramson Cancer Center, Perelman School of Medicine, University of Pennsylvania, Philadelphia, PA, 19104 USA

[7]Department of Neurosurgery, Perelman School of Medicine, University of Pennsylvania, Philadelphia, PA, 19104 USA

[8]Abramson Cancer Center, Perelman School of Medicine, University of Pennsylvania, Philadelphia, PA, 19104 USA

[9]Division of Hematology-Oncology, Department of Medicine, Perelman School of Medicine, University of Pennsylvania, Philadelphia, PA, 19104 USA

[10]Department of Pathology and Laboratory Medicine, Perelman School of Medicine, University of Pennsylvania, Philadelphia, PA, 19104 USA

[11]Warren Alpert Medical School of Brown University, Brown University, Providence, RI, 02903

Abstract

Glioblastoma (GBM) is an immunologically "cold" tumor characterized by poor responsiveness to immunotherapy. Standard-of-care for GBM is surgical resection followed by chemoradiotherapy and maintenance chemotherapy. However, tumor recurrence is the norm, and recurring tumors

‡ **Correspondence:** Gregory L. Beatty, MD, PhD, University of Pennsylvania, Perelman Center for Advanced Medicine, South Pavilion, Room 8-107, 3400 Civic Center Blvd., Philadelphia, PA 19104-5156, gregory.beatty@pennmedicine.upenn.edu, Cecile Alanio, MD, PhD, Deputy Director of the Clinical Immunology Laboratory at Institut Curie, Scientist in the U932 INSERM "Immunity and Cancer" Unit, Center for Cancer Immunotherapy, Hopital - 2ème Etage, 26 rue d'Ulm, 75248 Paris Cedex 05, France, cecile.alanio@curie.fr.

*Contributed equally

+Co-senior authors

are found frequently to have acquired molecular changes (e.g. mutations) that may influence their immunobiology. Here, we compared the immune contexture of *de novo* and recurrent GBM (rGBM) using high-dimensional cytometry and multiplex immunohistochemistry. Although myeloid and T cells were similarly abundant in *de novo* and rGBM, their spatial organization within tumors differed and was linked to outcomes. In rGBM, T cells were enriched and activated in perivascular regions and clustered with activated macrophages and fewer regulatory T cells. Moreover, higher expression of phosphorylated STAT1 by T cells in these regions at recurrence was associated with a favorable prognosis. Together, our data identify differences in the immunobiology of *de novo* and rGBM and identify perivascular T cells as potential therapeutic targets.

Keywords

Glioblastoma; tumor microenvironment; immune cells; spatial analyses

Introduction

Glioblastoma (GBM) is the most common primary malignant brain tumor in adults and is associated with a poor prognosis (1). Over the past 15 years, treatment options for GBM have shown little advancement. Standard-of-care treatment is surgical resection with adjuvant chemoradiotherapy followed by maintenance chemotherapy with temozolomide, an alkylating agent. However, with this approach, median overall survival is only 16.9 months and unfortunately, relapse is expected for nearly all patients (2).

Therapeutic resistance in GBM has been associated with tumor evolution. Genomic alterations are known to accumulate in response to temozolomide such that recurrent GBM (rGBM) displays a hypermutated phenotype compared to the initial tumor at diagnosis (*de novo*) (3,4). The quality of tumor-specific mutant peptides (neoantigens) present in rGBM along with T lymphocyte infiltrates identifies a subset of patients with a more favorable outcome (5). These findings raise the possibility that rGBM and *de novo* GBM differ immunologically, with potential implications for immunotherapy.

Immunotherapy has become a standard-of-care treatment for many solid cancers, yet therapeutic targeting of the immune system has not produced significant clinical benefit for most patients with GBM (6). This treatment resistance has been attributed to the ability of GBM to orchestrate an immunosuppressive tumor microenvironment and to a lack of immunogenic neoantigens expressed by tumor cells that have a low mutational burden in *de novo* GBM (7). Overall, GBM is defined as an immunologically “cold” tumor characterized by a paucity of tumor-infiltrating $CD3^+$ T cells but a strong presence of tumor-associated macrophages (8,9). The abundance of tumor-associated macrophages correlates with worse survival (8,9).

Several studies suggest that immune checkpoint blockade with anti–PD-1 as well as vaccines might trigger productive T-cell responses in some patients with GBM (10–13). These studies have been conducted in patients with rGBM and thus, the contribution of standard-of-care treatment to any immunological alterations detected remain undefined.

Thus, there is a strong need to examine the immune contexture of both *de novo* and rGBM to understand the immune response that occurs during GBM evolution.

Here, we performed deep cytometric profiling of tumor-infiltrating immune cells using mass cytometry and multiplex immunohistochemistry (mIHC) in *de novo* and rGBM surgical specimens to define the composition and distribution of immune-cell subsets detected in GBM tumor tissues. We found similar proportions of myeloid and T cells in *de novo* and rGBM, but differences in subsets across tumors, and substantial intratumoral heterogeneity in the spatial distribution of immune infiltrates. We identified increased numbers of $CD3^{+}pSTAT1^{+}$ cells in perivascular regions as associated with a longer median time from relapse to death. Collectively, our findings indicate that although both *de novo* and rGBM display potential targets for immunotherapy, rGBM might have a better potential for response to immunotherapies.

Methods

Patient and sample characteristics

Tumor samples were obtained from patients with GBM after written informed consent and de-identified. Peripheral blood mononuclear cells (PBMC) from healthy volunteers were obtained from the Human Immunology Core at the University of Pennsylvania, Studies were conducted in accordance with the 1996 Declaration of Helsinki and approved by the University of Pennsylvania's Institutional Review Board. For analysis by cytometry by time of flight (CyTOF), tumor samples were obtained from 27 patients (14 with *de novo* GBM and 13 with rGBM) after confirmation of a GBM diagnosis by a board-certified neuropathologist. Whole tumor was processed by mechanical and enzymatic dissociation using a gentleMACS™ Octo Dissociator in combination with the Brain Tumor Dissociation Kit (Miltenyi Biotec, cat no. 130–095-942) and then filtered through a 75mm strainer to generate a single-cell suspension. Samples were frozen in liquid nitrogen until further use. Characteristics of patients included in the CyTOF analysis are listed in Supplemental Table S1. For mIHC analyses, 17 patients who had previously had surgery for *de novo* and then rGBM performed at the University of Pennsylvania were identified through a medical records search. Unstained slides were cut at 5 μm thickness from formalin-fixed paraffin-embedded (FFPE) blocks for analysis. Characteristics of patients included in the mIHC analyses are listed in Supplemental Table S2 and the number of regions analyzed are detailed in Supplemental Table S3.

CyTOF

Thawed single-cell suspensions of tumor or healthy volunteer PBMC were assessed using CyTOF as previously described (14). Briefly, antibody panels (lymphoid, myeloid, and T cell) were designed to simultaneously measure the expression of molecules related to cell lineage, differentiation state, and function (Supplemental Table S4). Cells ($3x10^{6}$) were incubated with cisplatin for 1 minute, then stained at room temperature for 30 minutes with metal-labeled antibodies to detect surface proteins. Cells were then permeabilized using Fixation/Permeabilization solution (eBioscience, Thermo Fisher, cat no. 00–5123-43) at room temperature for 30 minutes and then stained at

room temperature for 60 minutes with metal-labeled antibodies to detect intracellular proteins. Cells were washed in permeabilization buffer and resuspended in PBS-1.6% paraformaldehyde before acquisition by CyTOF (Helios, Fluidigm). $CD45^+$ cells were identified as $Iridium^+Beads^-Cisplatin^-CD45^+$. Monocytes were identified as $CD3^-CD14^+$. B cells were identified as $CD3^-CD19^+$. NK cells were identified as $CD3^-CD56^+$. Mucosal associated invariant T (MAIT) cells were identified as $CD3^+CD161^+TCRV7.2^+$. T cell receptor gamma/delta (TCRgd) cells were identified as $CD3^+TCRgd^+$. Regulatory T (Treg) cells were identified as $CD3^+CD4^+CD25^+CD127^-$. Follicular helper T (TFH) cells were identified as $CD3^+CD4^+CXCR5^+PD\text{-}1^+$. Natural killer T (NKT) cells were identified as $CD3^+CD161^+TCRV24^+$. Analysis was performed using FlowJo v10 (TreeStar), as well as R v3.5.1 and RStudio v1.1.383. R scripts and other resources are available online at https://github.com/wherrylab/Cytof_analysis_calanio.

Microscopic analysis

FFPE tumor specimens were sectioned onto positively charged glass microscope slides. Automated mIHC was performed on a Ventana Discovery Ultra automated slide staining system (Roche). Slides were deparaffinized at 70°C for 24 minutes. Following deparaffinization, heat-induced epitope retrieval was performed using an EDTA-based preconditioning solution (Ventana Medical Systems, cat no. 950–500) for 64 minutes at 100°C. Slides were incubated with the appropriate primary and secondary antibodies prior to chromogenic signal detection using the regents and antibodies listed in Supplemental Table S5. Tissues were counterstained with hematoxylin (Ventana Medical Systems, cat no. 760–2021) and bluing reagent (Ventana Medical Systems, cat no. 760–2037). Whole slide scans of stained tissues were acquired at 40X using an Aperio CS2 scanner (Leica Biosystems).

mIHC image analysis

Scanned brightfield images were digitally quantified using custom image analysis algorithms. All algorithms were created using Visiopharm Integrator System (VIS) software (Version 2019.07). A board-certified neuropathologist identified and annotated areas of dense and infiltrative tumor from hematoxylin- and eosin-stained slides. Annotations were then transcribed onto scanned multiplex images. Areas of necrosis, non-neoplastic brain, predominantly reactive/treatment-related changes, and artifactual staining were excluded from analysis. Custom image analysis algorithms were applied to quantify the number of $CD3^+$, $CD3^+Ki\text{-}67^+$, $CD8^+$, $Foxp3^+$, $CD68^+$, $CD163^+$, $CD163^+Ki\text{-}67^+$, $EGFR^+p53^+$, $HLA\text{-}DR^+$, $HLA\text{-}DR^+CD68^+$, and $Ki\text{-}67^+$ cells within the neuropathologist-annotated areas of GBM. Thresholds were similarly applied across all samples to reduce variability. Each Visiopharm algorithm was reviewed to ensure reproducibility and to minimize error and variability with cell segmentation and with detection of cytoplasmic and nuclear features. Absolute cell counts were normalized to the total area of the annotations and reported as densities (cells per mm^2).

To visualize the quantity and distribution of $CD8^+$ lymphoid aggregates in paired *de novo* and rGBM specimens, heat maps based on the density of $CD8^+$ cells present within a 100μm drawing radius were generated on annotated tissues. Standardized minimum and

maximum thresholds were applied during heatmap generation to allow for comparisons among specimens.

Separately, to facilitate the unbiased selection of T-cell high and T-cell low regions, individual regions-of-interest (ROIs) were delineated around areas of low and high density identified from the heat map. ROI sizes were determined by overall areas of identified tumor. These ROIs were carried over to annotate the identical T-cell low and T-cell high regions on serial sections of tissues that were stained for additional immune markers. All quantitative measurements were normalized to the area of the ROIs. To quantify the number of T-cell high loci per case, 1,035 by 1,035 μm square grids were superimposed upon CD8 density heatmaps. The number of grids containing CD8-enriched hotspots was quantified and expressed as a percentage of the total number of grids.

Statistical analyses

For group comparisons and correlation analyses, testing was performed using PRISM 8.4 (GraphPad Software). Normality of distributions was assessed using D'Agostino–Pearson omnibus normality test and variance between groups of data was determined using the *F*-test. For non-normal data, non-parametric Mann–Whitney *U*-tests were used for unpaired analyses. Descriptive statistics included mean, median, standard deviation and range for continuous variables and frequency and proportion for categorical variables. For survival discrimination, unsupervised k-means clustering (k=2) was used to stratify patients into two groups based on overall survival, via the *kmeans* command in the *stats* suite of commands on R (version 3.5.3). 10 random starts and 1,000 maximum iterations were used as parameters. K-means clustering demonstrated successful convergence, with stratification of patients into two distinct survival groups minimizing within-cluster variance (between-cluster sum of squares / total sum of squares = 0.701). Cluster analysis was also re-performed with kernel density estimation using the *pdfCluster* package on R, which determines the optimal number of clusters and partitions variables via nonparametric density estimation. The same survival group assignments were reached through kernel density estimation.

Analyses correlating gene expression and patient survival used the maximal selected rank statistics package (maxstat on R) according to prior studies (9). This methodology was used to select the optimal cutoff for dichotomizing a quantitative predictor, such as gene expression, into high and low groups, when analyzed in association with a quantitative response, such as survival. Subsequently, Kaplan-Meier curves were generated for high- and low-expression groups and differences in survival were quantified via the maximally selected rank test and independent t-tests. Statistical significance was defined as $P<0.05$.

Data availability statement

The data generated in this study are available within the article and its supplementary data files or from the corresponding authors upon reasonable request.

Results

Evaluation of immune contexture in de novo and recurrent human GBM

To examine the immune infiltrate of human GBM, we performed deep single-cell immune profiling of tumors using mass CyTOF. We evaluated human GBM surgical specimens collected on unmatched patients with *de novo* (n=14) or rGBM (n=13) (Figure 1A, Supplemental Table S1). All rGBM patients had received standard-of-care therapy, comprised of concurrent radio- and chemotherapy, followed by maintenance chemotherapy with temozolomide. Three rGBM patients (010, 012, and 065) received experimental treatment on a clinical trial after completing standard-of-care therapy (Supplementary Table S1).

We used three CyTOF antibody panels (myeloid, lymphoid, and T cell) to measure the expression of up to 40 molecules by tumor-infiltrating immune cells (Supplemental Table S4). All samples were analyzed using a T-cell panel, but due to insufficient material from some samples, analysis with either a myeloid or lymphoid panel was limited to only a subset of patients (*de novo,* n=5 and rGBM, n=5 for myeloid panel; *de novo*, n=10 and rGBM, n=9 for lymphoid panel). Using this approach, we found that the $CD45^+$ leukocyte infiltrate seen in GBM tissues consisted primarily of myeloid cells (~60% of $CD45^+$ hematopoietic cells) and T cells (~20%) (Figure 1B–D). Proportions of myeloid cells and T cells were similar in *de novo* and rGBM (Figure 1B–D, Supplemental Table S6). Other cells detected included B cells (~6%), NK cells (~4%), MAIT cells (~1%), TCRgd cells (~1%), and rare NKT cells (~0.05%) (Supplemental Figure S1A).

A more detailed analysis of $CD45^+$ myeloid cells identified three major subsets. The *Myeloid I* subset was the most abundant and expressed CD64, CD11b, HLA-DR, CD80, and low levels of CD14 but lacked expression of CD68 and CD163 (Figure 1E and Supplemental Figure S1B). As such, *Myeloid I* resembled tissue-resident microglial-derived tumor-associated macrophages (TAM) (15,16). The *Myeloid II* subset expressed CD68, HLA-DR, CD1c, CD14, CD15, CD163, CD40, and CD73, but lacked expression of costimulatory molecules including CD80 and CD86. As such, *Myeloid II* is consistent with a mixture of type-1 myeloid dendritic cells (cDC1) and $CD163^{hi}$ monocyte-derived TAM (15,16). Finally, the *Myeloid III* subset expressed CD68, CD24, CD14, CD80, and low CD163 but lacked expression of HLA-DR (Figure 1E and Supplemental Figure S1B). As such, *Myeloid III* resembled $CD163^{low}$ monocyte-derived TAM (15,16). Overall, the proportion of Myeloid I, II and III subsets varied among patients and between *de novo* and rGBM tumors, with a tendency for more monocyte-derived (Myeloid II and III) and less tissue-resident (Myeloid I) TAM in the recurrent cases (Figure 1E). The overall proportions of cells expressing CD163, HLA-DR, CD80, and CD86 were largely equivalent between *de novo* and rGBM tumors except for a slight increase in the proportion of CD80-expressing myeloid cells detected in *de novo* tumors (p=0.01, Figure 1F). The latter may relate to the increased abundance of CD80-expressing cells in the *Myeloid I* subset seen in the *de* novo setting (Figure 1G). As such, although myeloid cells were equally abundant in *de novo* and rGBM tumors, their subset composition appeared to differ with increased abundance of monocyte-derived macrophages in rGBM tumors.

Given that T cells are key mediators of antitumor activity in response to immunotherapy, we next examined T-cell composition in GBM tumors. Overall, the frequency of $CD8^+$ T cells was similar for *de novo* and rGBM. However, *de novo* tumors contained a higher frequency of $CD4^+$ T cells (~35% versus 20% in rGBM) (Figure 1H). $CD4^+$ T cells for *de novo* and recurrent tumors were comprised of similar proportions of $CD25^+CD127^-$ Treg cells (~15%) (Supplemental Figure S1C) and $CXCR5^+PD\text{-}1^+$ TFH cells (~15%) (Supplemental Figure S1D), indicating that the increased frequency of $CD4^+$ T cells may relate to an increase in conventional $CD4^+$ T cells in *de novo* tumors. The majority of conventional $CD8^+$ T cells expressed PD-1 (~80%), in both *de novo* and rGBM tumors (Supplemental Figure S2A & S2B). PD-1 expressing $CD8^+$ T cells also co-expressed multiple co-inhibitory immune checkpoints such as TIM-3, LAG-3, and CTLA4, consistent with a substantial proportion of exhausted $CD8^+$ T cells (TEX) infiltrating human GBM (Figure 1I) (17). In both *de novo* and rGBM, ~60% of $CD8^+$ T cells also expressed both PD-1 and CD39, a combination associated with TEX cells and previously implicated as identifying tumor-reactive T cells in other settings (18) (Supplemental Figure S2C & S2D).

In settings of chronic infection or cancer in mice, populations of progenitor TEX cells ($CXCR5^+CD69^{+/-}$), transitional or intermediate TEX cells ($CXCR5^-CD69^-$), and terminal TEX cells ($CXCR5^-CD69^+$) have been defined with distinct functional properties (19–23). For example, progenitor TEX cells have a key role in response to immune checkpoint blockade (24–26). In addition, progenitor TEX cells contain the highest frequency of IFNg and TNF producers and are the subset of TEX cells that undergoes proliferative expansion in response to PD-1 pathway blockade (19). In contrast, intermediate TEX cells contain more migratory cells that are in cell cycle and are derived from progenitor TEX cells. Intermediate TEX cells eventually transition to terminal TEX cells that display features of tissue residency (19,20,23). Based on this biology, we evaluated expression of CXCR5 and CD69 on $PD\text{-}1^+CD8^+$ T cells in GBM tumors. In both *de novo* and rGBM, approximately 60–75% of $PD\text{-}1^+CD8^+$ T cells expressed CXCR5 with about 50% expressing CD69. In addition, most $CD69^+CD8^+$ T cells co-expressed CXCR5 with 10–15% lacking CXCR5 (Supplemental Figure S3A & S3B). This pattern is suggestive of a predominantly progenitor TEX–cell phenotype detected in GBM tumors (19,27). Thus, our data show that $CD8^+$ T-cell infiltrates in GBM are likely to be tumor-reactive based on high PD-1 and CD39 co-expression (18) and exist predominantly in a progenitor TEX cell state.

Perivascular immune communities distinguish de novo and rGBM

Although myeloid and T cells appeared to be similarly abundant phenotypically between *de novo* and rGBM, we hypothesized that their spatial distribution may be altered. To explore this possibility, we performed mIHC on 17 paired *de novo* and rGBM tumor tissues (Supplemental Table S2). Here, we focused our analyses on ROIs containing tumor, an approach that contrasts with our CyTOF studies, which examined cells present throughout the entire tumor tissue specimen. Despite this difference, mIHC revealed a similar overall content of tumor-infiltrating $CD8^+$ T cells in the paired *de novo* and rGBM samples (Figure 2A). $CD8^+$ T cells were detected throughout the tumor microenvironment, but the density of $CD8^+$ T cells was greatest in perivascular regions for both *de novo* and rGBM (Figure 2B), consistent with previous findings (28). Visual examination of CD8 staining showed

qualitative differences in the distribution of $CD8^+$ T cells between paired *de novo* and rGBM samples (Figure 2C). This difference was due to an increased number of perivascular regions associated with $CD8^+$ T cells seen in rGBM samples compared to paired *de novo* samples (Figure 2D) and appeared to be independent of sex as a biological variable (Supplemental Figure S4).

Next, we applied a series of mIHC panels and computer-assisted image analysis algorithms to define the immune microenvironment of perivascular T cell–enriched regions present in the setting of rGBM (Figure 2E, Supplemental Figure S5). Heatmaps displaying the density of $CD8^+$ cells in tumor regions (Figure 2C) were used to define $CD8^+$ T-cell low ("T-cell low") and $CD8^+$ T-cell high ("T-cell high") regions (Supplemental Table S7). This approach identified proliferating T cells, as defined by Ki67 expression, mainly in T-cell high regions in rGBM (Figure 2F, G). In addition, pSTAT1 expression, a marker of interferon signaling, was frequently associated with T-cell high regions, although some rGBM samples lacked pSTAT1 expression and not all T-cell high regions associated with pSTAT1 (Figure 2F, G). Similarly, the myeloid compartment in T-cell high regions was enriched in $HLA\text{-}DR^+$ and $pSTAT1^+$ myeloid cells (Figure 2F, H). In contrast, the density of $CD68^+$ macrophages that lacked HLA-DR was similar between T-cell low and T-cell high regions in rGBM samples (Supplemental Figure S6).

We next asked whether immune features present within T-cell high regions differed between *de novo* and rGBM. Perivascular T-cell high regions in rGBM displayed a lower density of $FOXP3^+$ Treg cells and a significantly higher ratio of $CD8^+$ T cells to $FOXP3^+$ Treg cells compared to T-cell high regions in *de novo* GBM (Figure 2I, J). Moreover, some perivascular T-cell high regions in rGBM also showed a higher expression of $pSTAT1^+$ cells compared to perivascular T-cell high regions in *de novo* GBM, although this comparison did not meet statistical significance ($P = 0.08$) (Figure 2K, L). Collectively, these data suggest that rGBM displays features of an immunologically active tumor that are distinct from the *de novo* tumor, particularly in the perivascular regions where immune cells may accumulate.

Immunological features associated with perivascular regions correlate with clinical outcomes

A key question is whether intra- or peri-tumoral immune features have any relationship to disease outcomes. Thus, we next examined the relationship between immune features present in T-cell high regions in rGBM and survival outcomes. Patients were dichotomized into either short-term survivors (STS) or long-term survivors (LTS) using an unsupervised k-means clustering algorithm based on the median overall survival from time of diagnosis (Figure 3A). The median overall survival in the STS group was 11.5 months and in the LTS group was 27.5 months ($P<0.0001$). In the LTS group, T-cell high regions contained significantly fewer cells expressing Ki-67 (Figure 3B, C). To investigate whether this Ki-67 difference reflected changes in tumor-cell proliferation, we excluded proliferating T cells ($CD3^+Ki\text{-}67^+$) and macrophages ($CD163^+Ki\text{-}67^+$) from the total population of $Ki\text{-}67^+$ cells detected in T-cell high regions. Consistent with prior work (29), the residual $CD3^-CD163^-Ki\text{-}67^+$ population, presumably composed primarily of tumor cells, showed the same Ki-67 relationship with survival, with the LTS cohort exhibiting lower numbers of

Ki-67$^+$ tumor cells in T-cell high regions (Figure 3C). T-cell high regions in LTS patients also were enriched in CD68$^+$ and HLA-DR$^+$CD68$^+$ macrophages (Figure 3D & 3E). Of note, LTS patients displayed a significantly higher density of pSTAT1$^+$ cells but the density of CD3$^+$ cells co-expressing pSTAT1 did not reach significance (Figure 3F & 3G). Taken together, these data suggest that the immunologic microenvironment of T-cell high regions in rGBM may harbor prognostic value for overall survival.

To further examine the relationship between spatial immune microenvironmental features and disease outcome, we evaluated immunological features defined by the mIHC analyses and their association with clinical outcomes in rGBM. To do this, we stratified patients with rGBM (Supplemental Table S2) into two groups using the maximal selected rank statistics approach based on all expression features individually. We then tested their association with survival using log-rank tests and corrected for multiple testing. The CD3$^+$pSTAT1$^+$ binary classification (low vs high) identified 6 patients with high expression and 8 patients with low expression. Although no difference in overall survival was observed based on this classification, patients in the CD3$^+$pSTAT1$^+$ high group had a longer median time from relapse to death (high, 10 months; low, 4 months; p=0.0223, Figure 4). This extended time to relapse was confirmed in a Cox proportional-hazards model including age, sex, Ki67, MGMT, EGFR, TP53, and extent of resection at *de novo* status as predictor variables (for CD3$^+$pSTAT1$^+$ p=0.0223). These data suggest that the T-cell compartment, especially in the perivascular regions of the tumor, in some patients with rGBM may be polarized toward an antitumor activated phenotype with clinical implications.

Discussion

In this study, we examined contextual and spatial differences in the immune landscape of *de novo* and rGBM tumors and identified immunological features with potential clinical implications. Using mass cytometry, myeloid cells and T cells were found to be similarly present in *de novo* and rGBM. Myeloid cells were the most abundant cells in the tumor microenvironment and were accompanied by infiltrating TEX cells, consistent with prior studies (30–32). This finding is also consistent with recent work comparing the microenvironmental landscape in glioma and brain metastases (15,16). In these studies, the myeloid cell composition of gliomas was shown to be markedly heterogeneous and was composed of tissue-resident and infiltrating leukocytes. Our study is consistent with these reports and provides new insights into variations in the leukocyte infiltrate present in *de novo* and rGBM. For example, we identified differences in the composition of myeloid subsets detected in *de novo* and rGBM samples. Although we were not able to definitively distinguish between tissue-resident and monocyte-derived macrophages in our studies (15,16), rGBM tended to have an increased frequency of myeloid cells that resembled monocyte-derived macrophages. Prior studies have shown that a high infiltration of monocyte-derived macrophages associates with poor survival in GBM patients (15). In contrast, *de novo* GBM tended to have an increased frequency of myeloid cells that resembled tissue-resident macrophages. It is possible that these differences reflect response to standard-of-care therapy (33). Alternatively, they may indicate cancer cell–intrinsic differences between *de novo* and rGBM tumors that differentially shape the recruitment and *in situ* differentiation of monocyte-derived macrophages.

Differences in T-cell subsets were also observed between *de novo* and rGBM. With deep profiling, TEX cells were detected in both *de novo* and rGBM, with most of these cells expressing CXCR5, as well as potential therapeutic targets such as PD-1, LAG-3 and CTLA-4. Notably, these TEX cells expressed CD39 together with PD-1, suggesting that they may be tumor reactive (18). Using mIHC, we then further tested if the spatial distribution of infiltrating immune cells differed between *de novo* and rGBM. T-cell high perivascular regions were more abundant in rGBM compared to *de novo* GBM and differentially displayed markers of immune activation (pSTAT1) and cellular proliferation (Ki67). Increased numbers of $CD3^{+}pSTAT1^{+}$ cells in perivascular regions associated with a longer median time from relapse to death. Taken together, our findings identify the spatial distribution of T cells rather than their abundance as a potential key immunological determinant that associates with the evolution and pathogenesis of GBM.

Immune infiltration is a recognized determinant of outcomes in cancer. In *de novo* GBM, myeloid-cell infiltrates associate with an unfavorable prognosis (8,9). In contrast, variable correlations with survival have been reported for T-cell infiltrates (9,34). However, less is known about the immunological features of rGBM, where tumors are known to have acquired molecular alterations, including increased alternative-splicing events, that may influence tumor immunogenicity (35). Here, our studies identified distinct spatial organization and activation characteristics of immune cells in *de novo* versus rGBM tumors. Specifically, T cell–enriched perivascular regions were more abundant in rGBM compared to *de novo* GBM. Perivascular spaces have been recently identified as lymphopoietic niches at the central nervous system border (36,37). It is also known that the perivascular space is important for maintaining the self-renewal and stemness of cancer cells (38,39). Our findings suggest that enrichment of activated T cells in perivascular regions may be a determinant of longer survival in patients with rGBM. This observation raises the possibility that tumor-reactive T cells in perivascular regions may control the fate of glioma stem cells. Consistent with this idea, cytotoxic T cells engineered to recognize tumor antigens (e.g. HER2 and NKG2D ligands) or redirected against CD133, a marker of stem cells, have shown antitumor activity against glioma stem cells (40–42). However, it remains unclear whether endogenous tumor-reactive T cells are present in perivascular regions and capable of eliminating glioma stem cells in patients. In contrast, prior studies have shown that glioma stem cells can suppress T-cell proliferation and activation (43). Nonetheless, manipulating the perivascular niche may be a strategy to leverage the antitumor potential of infiltrating leukocytes (44).

Our findings of abundant T cell–enriched perivascular regions in rGBM may indicate their potential role in response to therapeutic interventions. In line with this idea, we found that T-cell activation in the perivascular region associated with increased time from relapse to death. Specifically, a high density of $CD3^{+}$ T cells expressing pSTAT1 was found suggesting recent signaling from interferons or other inflammatory mediators. Interferons can have antitumor activity but may also support immune evasion by triggering the upregulation of immune checkpoint molecules (45). In GBM, interferon signaling has been previously associated with a poor prognosis (46). However, our data differ from these analyses given that we focused on pSTAT1 expression in T cell–enriched regions of GBM. It

will be important in subsequent analyses to better understand the signaling programs that distinguish T cell–enriched regions defined by high and low pSTAT1 expression.

Perivascular regions in GBM are associated with monocyte-derived macrophages, which portend a poor outcome (15). TAMs in these regions support tumor growth by producing soluble factors that sustain glioma stemness (47). However, we found that an increased density of $CD68^+$ myeloid cells expressing HLA-DR associated with increased survival. These changes seen in the activation status of both myeloid cells and T cells may reflect antitumor immune activity and/or treatment-induced inflammation. In addition, we found that not all perivascular regions were infiltrated by T cells in rGBM, and the degree of infiltration was variable between patients, thereby illustrating both intra- and inter-patient heterogeneity in the immune response to GBM. Analyses of intercellular communications and the phenotypical state of cells in perivascular regions after various treatment regimens are warranted.

Our studies were conducted in a small cohort of patients with *de novo* and rGBM and thus, may not be representative of all subsets of GBM. Our analyses also assessed only a small cross-sectional tumor region of GBM for each patient raising the possibility of sampling bias due to the prominent intratumoral heterogeneity that is characteristic of GBM. In addition, our studies addressed defined timepoints, namely surgical resection for *de novo* and recurrent GBM, and thus, did not address the dynamics of GBM pathogenesis. In this regard, diagnostic imaging strategies that incorporate tissue biomarkers may enable a whole lesion assessment and permit non-invasive longitudinal analyses.

Immunotherapy has yet to reproducibly demonstrate activity in GBM. For example, monotherapy with pembrolizumab has shown minimal benefit so far (48). However, recent work suggests that combining immune checkpoint blockade (e.g. anti-PD-1) with tumor vaccines might trigger productive T-cell responses in some patients with GBM (10–13). These studies have all been conducted in patients with rGBM and whether targeting *de novo* tumors would be more impactful is unclear. Our findings revealed abundant T cell–enriched perivascular regions in rGBM and show that immune activation associates with delayed disease progression. Thus, we propose that rGBM may have a greater potential for response to immunotherapies.

In summary, our study identifies the perivascular space as a potential immune determinant of GBM biology. Specifically, increased T-cell infiltration into perivascular regions was seen in rGBM compared to *de novo* GBM and T-cell activation in perivascular regions correlated with improved outcomes. Thus, the perivascular space in GBM may be a key immunological target with therapeutic implications.

Supplementary Material

Refer to Web version on PubMed Central for supplementary material.

Acknowledgements:

The authors thank members of the Wherry, O'Rourke, and Beatty laboratories for critical feedback, the Pathology Clinical Service Center of Penn Medicine for sample acquisition and slide cutting, and the Glioblastoma Translational Center of Excellence for coordinating the work. The authors also acknowledge and thank the patients from whom tissue samples were donated and made this study feasible.

Conflict of Interests: G.L.B. reports prior or active roles as a consultant/advisory board member for Seagen, Boehinger Ingelheim, Cour Pharmaceuticals, Adicet Bio, Aduro Biotech, AstraZeneca, BioMarin Pharmaceuticals, Bristol-Myers Squibb, Genmab, Hibercell, Incyte, Cantargia, Janssen, Opsona, Merck, Monopteros, Molecular Partners, Nano Ghosts, Pancreatic Cancer Action Network, Shattuck Labs, Verastem, and BiolineRx; reports receiving commercial research grants from Incyte, Bristol-Myers Squibb, Verastem, Halozyme, Biothera, Hibercell, Newlink, Novartis, Genmab, Arcus, and Janssen. G.L.B. is an inventor of intellectual property (U.S. patent numbers 10,640,569 and 10,577,417) and recipient of royalties related to CAR T cells that is licensed by the University of Pennsylvania to Novartis and Tmunity Therapeutics. E.J.W. has consulting agreements with and/or is on the scientific advisory board for Merck, Marengo, Janssen, Related Sciences, Rubius Therapeutics, Synthekine and Surface Oncology. E.J.W. is a founder of Danger Bio, Surface Oncology and Arsenal Biosciences and also has a patent licensing agreement on the PD-1 pathway with Roche/Genentech. Z.A.B. and D.M.O. are on patent filings related to CAR T cells. D.M.O. receives monetary support from Tmunity Therapeutics for unrelated lab work. D.M.O is an inventor of intellectual property on patents licensed by the University of Pennsylvania to Tmunity.

Funding:

The study and analyses were funded by R01-CA197916 (G.L.B.), The GBM Translational Center of Excellence (Z.A.B., L.Z., J.V.Z., D.M.O.), The Templeton Family Initiative in Neuro-Oncology (D.M.O.), The Maria and Gabriele Troiano Brain Cancer Immunotherapy Fund (D.M.O.), and the Neurosurgery Research & Education Foundation (O.Y.T.). E.J.W. was supported by NIH grants CA016520, CA210944, AI149680, AI155577, AI108545, and AI082630. E.J.W. and C.A. were also supported by the Parker Institute for Cancer Immunotherapy which supports the cancer immunology program at the University of Pennsylvania.

References

1. Marenco-Hillembrand L, Wijesekera O, Suarez-Meade P, Mampre D, Jackson C, Peterson J, et al. Trends in glioblastoma: outcomes over time and type of intervention: a systematic evidence based analysis. J Neurooncol 2020;147(2):297–307. [PubMed: 32157552]
2. Lara-Velazquez M, Shireman JM, Lehrer EJ, Bowman KM, Ruiz-Garcia H, Paukner MJ, et al. A Comparison Between Chemo-Radiotherapy Combined With Immunotherapy and Chemo-Radiotherapy Alone for the Treatment of Newly Diagnosed Glioblastoma: A Systematic Review and Meta-Analysis. Front Oncol 2021;11:662302. [PubMed: 34046356]
3. Johnson BE, Mazor T, Hong C, Barnes M, Aihara K, McLean CY, et al. Mutational analysis reveals the origin and therapy-driven evolution of recurrent glioma. Science 2014;343(6167):189–93. [PubMed: 24336570]
4. Barthel FP, Johnson KC, Varn FS, Moskalik AD, Tanner G, Kocakavuk E, et al. Longitudinal molecular trajectories of diffuse glioma in adults. Nature 2019;576(7785):112–20. [PubMed: 31748746]
5. Zhang J, Caruso FP, Sa JK, Justesen S, Nam DH, Sims P, et al. The combination of neoantigen quality and T lymphocyte infiltrates identifies glioblastomas with the longest survival. Commun Biol 2019;2:135. [PubMed: 31044160]
6. Omuro A, Vlahovic G, Lim M, Sahebjam S, Baehring J, Cloughesy T, et al. Nivolumab with or without ipilimumab in patients with recurrent glioblastoma: results from exploratory phase I cohorts of CheckMate 143. Neuro Oncol 2018;20(5):674–86. [PubMed: 29106665]
7. Sha D, Jin Z, Budczies J, Kluck K, Stenzinger A, Sinicrope FA. Tumor Mutational Burden as a Predictive Biomarker in Solid Tumors. Cancer Discov 2020;10(12):1808–25. [PubMed: 33139244]
8. Haddad AF, Chen JS, Oh T, Pereira MP, Joshi RS, Aghi MK. Higher cytolytic score correlates with an immunosuppressive tumor microenvironment and reduced survival in glioblastoma. Sci Rep 2020;10(1):17580. [PubMed: 33067480]
9. Marinari E, Allard M, Gustave R, Widmer V, Philippin G, Merkler D, et al. Inflammation and lymphocyte infiltration are associated with shorter survival in patients with high-grade glioma. Oncoimmunology 2020;9(1):1779990. [PubMed: 32923142]

10. Schalper KA, Rodriguez-Ruiz ME, Diez-Valle R, Lopez-Janeiro A, Porciuncula A, Idoate MA, et al. Neoadjuvant nivolumab modifies the tumor immune microenvironment in resectable glioblastoma. Nat Med 2019;25(3):470–6. [PubMed: 30742120]
11. Zhao J, Chen AX, Gartrell RD, Silverman AM, Aparicio L, Chu T, et al. Immune and genomic correlates of response to anti-PD-1 immunotherapy in glioblastoma. Nat Med 2019;25(3):462–9. [PubMed: 30742119]
12. Keskin DB, Anandappa AJ, Sun J, Tirosh I, Mathewson ND, Li S, et al. Neoantigen vaccine generates intratumoral T cell responses in phase Ib glioblastoma trial. Nature 2019;565(7738):234–9. [PubMed: 30568305]
13. Hilf N, Kuttruff-Coqui S, Frenzel K, Bukur V, Stevanovic S, Gouttefangeas C, et al. Actively personalized vaccination trial for newly diagnosed glioblastoma. Nature 2019;565(7738):240–5. [PubMed: 30568303]
14. O'Boyle KC, Ohtani T, Manne S, Bengsch B, Henrickson SE, Wherry EJ, et al. Exploration of T-Cell Diversity Using Mass Cytometry. Methods Mol Biol 2020;2111:1–20. [PubMed: 31933194]
15. Friebel E, Kapolou K, Unger S, Nunez NG, Utz S, Rushing EJ, et al. Single-Cell Mapping of Human Brain Cancer Reveals Tumor-Specific Instruction of Tissue-Invading Leukocytes. Cell 2020;181(7):1626–42. [PubMed: 32470397]
16. Klemm F, Maas RR, Bowman RL, Kornete M, Soukup K, Nassiri S, et al. Interrogation of the Microenvironmental Landscape in Brain Tumors Reveals Disease-Specific Alterations of Immune Cells. Cell 2020;181(7):1643–60. [PubMed: 32470396]
17. Woroniecka K, Chongsathidkiet P, Rhodin K, Kemeny H, Dechant C, Farber SH, et al. T-Cell Exhaustion Signatures Vary with Tumor Type and Are Severe in Glioblastoma. Clin Cancer Res 2018;24(17):4175–86. [PubMed: 29437767]
18. Duhen T, Duhen R, Montler R, Moses J, Moudgil T, de Miranda NF, et al. Co-expression of CD39 and CD103 identifies tumor-reactive CD8 T cells in human solid tumors. Nat Commun 2018;9(1):2724. [PubMed: 30006565]
19. Beltra JC, Manne S, Abdel-Hakeem MS, Kurachi M, Giles JR, Chen Z, et al. Developmental Relationships of Four Exhausted CD8(+) T Cell Subsets Reveals Underlying Transcriptional and Epigenetic Landscape Control Mechanisms. Immunity 2020;52(5):825–41. [PubMed: 32396847]
20. Hudson WH, Gensheimer J, Hashimoto M, Wieland A, Valanparambil RM, Li P, et al. Proliferating Transitory T Cells with an Effector-like Transcriptional Signature Emerge from PD-1(+) Stem-like CD8(+) T Cells during Chronic Infection. Immunity 2019;51(6):1043–58. [PubMed: 31810882]
21. Miller BC, Sen DR, Al Abosy R, Bi K, Virkud YV, LaFleur MW, et al. Subsets of exhausted CD8(+) T cells differentially mediate tumor control and respond to checkpoint blockade. Nat Immunol 2019;20(3):326–36. [PubMed: 30778252]
22. Alanio C, Wherry EJ. Subsetting the subsets: Heterogeneity and developmental relationships of T cells in human tumors. Sci Immunol 2021;6(61):abj3067.
23. Zander R, Schauder D, Xin G, Nguyen C, Wu X, Zajac A, et al. CD4(+) T Cell Help Is Required for the Formation of a Cytolytic CD8(+) T Cell Subset that Protects against Chronic Infection and Cancer. Immunity 2019;51(6):1028–42. [PubMed: 31810883]
24. Blackburn SD, Shin H, Freeman GJ, Wherry EJ. Selective expansion of a subset of exhausted CD8 T cells by alphaPD-L1 blockade. Proc Natl Acad Sci U S A 2008;105(39):15016–21. [PubMed: 18809920]
25. Im SJ, Konieczny BT, Hudson WH, Masopust D, Ahmed R. PD-1+ stemlike CD8 T cells are resident in lymphoid tissues during persistent LCMV infection. Proc Natl Acad Sci U S A 2020;117(8):4292–9. [PubMed: 32034098]
26. Sade-Feldman M, Yizhak K, Bjorgaard SL, Ray JP, de Boer CG, Jenkins RW, et al. Defining T Cell States Associated with Response to Checkpoint Immunotherapy in Melanoma. Cell 2018;175(4):998–1013. [PubMed: 30388456]
27. Simoni Y, Becht E, Fehlings M, Loh CY, Koo SL, Teng KWW, et al. Bystander CD8(+) T cells are abundant and phenotypically distinct in human tumour infiltrates. Nature 2018;557(7706):575–9. [PubMed: 29769722]

28. Mu L, Yang C, Gao Q, Long Y, Ge H, DeLeon G, et al. CD4+ and Perivascular Foxp3+ T Cells in Glioma Correlate with Angiogenesis and Tumor Progression. Front Immunol 2017;8:1451. [PubMed: 29163521]
29. Bagley SJ, Schwab RD, Nelson E, Viaene AN, Binder ZA, Lustig RA, et al. Histopathologic quantification of viable tumor versus treatment effect in surgically resected recurrent glioblastoma. J Neurooncol 2019;141(2):421–9. [PubMed: 30446903]
30. Mohme M, Schliffke S, Maire CL, Runger A, Glau L, Mende KC, et al. Immunophenotyping of Newly Diagnosed and Recurrent Glioblastoma Defines Distinct Immune Exhaustion Profiles in Peripheral and Tumor-infiltrating Lymphocytes. Clin Cancer Res 2018;24(17):4187–200. [PubMed: 29444930]
31. Fu W, Wang W, Li H, Jiao Y, Huo R, Yan Z, et al. Single-Cell Atlas Reveals Complexity of the Immunosuppressive Microenvironment of Initial and Recurrent Glioblastoma. Front Immunol 2020;11:835. [PubMed: 32457755]
32. Gonzalez-Tablas Pimenta M, Otero A, Arandia Guzman DA, Pascual-Argente D, Ruiz Martin L, Sousa-Casasnovas P, et al. Tumor cell and immune cell profiles in primary human glioblastoma: Impact on patient outcome. Brain Pathol 2021;31(2):365–80. [PubMed: 33314398]
33. Ye Z, Ai X, Zhao L, Fei F, Wang P, Zhou S. Phenotypic plasticity of myeloid cells in glioblastoma development, progression, and therapeutics. Oncogene 2021;40(42):6059–70. [PubMed: 34556813]
34. Kmiecik J, Poli A, Brons NH, Waha A, Eide GE, Enger PO, et al. Elevated CD3+ and CD8+ tumor-infiltrating immune cells correlate with prolonged survival in glioblastoma patients despite integrated immunosuppressive mechanisms in the tumor microenvironment and at the systemic level. J Neuroimmunol 2013;264(1–2):71–83. [PubMed: 24045166]
35. Wang L, Shamardani K, Babikir H, Catalan F, Nejo T, Chang S, et al. The evolution of alternative splicing in glioblastoma under therapy. Genome Biol 2021;22(1):48. [PubMed: 33499924]
36. Cugurra A, Mamuladze T, Rustenhoven J, Dykstra T, Beroshvili G, Greenberg ZJ, et al. Skull and vertebral bone marrow are myeloid cell reservoirs for the meninges and CNS parenchyma. Science 2021;373(6553):eabf7844. [PubMed: 34083447]
37. Brioschi S, Wang WL, Peng V, Wang M, Shchukina I, Greenberg ZJ, et al. Heterogeneity of meningeal B cells reveals a lymphopoietic niche at the CNS borders. Science 2021;373(6553):eabf9277. [PubMed: 34083450]
38. Beck B, Driessens G, Goossens S, Youssef KK, Kuchnio A, Caauwe A, et al. A vascular niche and a VEGF-Nrp1 loop regulate the initiation and stemness of skin tumours. Nature 2011;478(7369):399–403. [PubMed: 22012397]
39. Calabrese C, Poppleton H, Kocak M, Hogg TL, Fuller C, Hamner B, et al. A perivascular niche for brain tumor stem cells. Cancer Cell 2007;11(1):69–82. [PubMed: 17222791]
40. Ahmed N, Salsman VS, Kew Y, Shaffer D, Powell S, Zhang YJ, et al. HER2-specific T cells target primary glioblastoma stem cells and induce regression of autologous experimental tumors. Clin Cancer Res 2010;16(2):474–85. [PubMed: 20068073]
41. Prasad S, Gaedicke S, Machein M, Mittler G, Braun F, Hettich M, et al. Effective Eradication of Glioblastoma Stem Cells by Local Application of an AC133/CD133-Specific T-cell-Engaging Antibody and CD8 T Cells. Cancer Res 2015;75(11):2166–76. [PubMed: 25840983]
42. Yang D, Sun B, Dai H, Li W, Shi L, Zhang P, et al. T cells expressing NKG2D chimeric antigen receptors efficiently eliminate glioblastoma and cancer stem cells. J Immunother Cancer 2019;7(1):171. [PubMed: 31288857]
43. Wei J, Barr J, Kong LY, Wang Y, Wu A, Sharma AK, et al. Glioblastoma cancer-initiating cells inhibit T-cell proliferation and effector responses by the signal transducers and activators of transcription 3 pathway. Mol Cancer Ther 2010;9(1):67–78. [PubMed: 20053772]
44. Wang Q, He Z, Huang M, Liu T, Wang Y, Xu H, et al. Vascular niche IL-6 induces alternative macrophage activation in glioblastoma through HIF-2alpha. Nat Commun 2018;9(1):559. [PubMed: 29422647]
45. Castro F, Cardoso AP, Goncalves RM, Serre K, Oliveira MJ. Interferon-Gamma at the Crossroads of Tumor Immune Surveillance or Evasion. Front Immunol 2018;9:847. [PubMed: 29780381]

46. Zhu C, Zou C, Guan G, Guo Q, Yan Z, Liu T, et al. Development and validation of an interferon signature predicting prognosis and treatment response for glioblastoma. Oncoimmunology 2019;8(9):e1621677. [PubMed: 31428519]

47. Shi Y, Ping YF, Zhou W, He ZC, Chen C, Bian BS, et al. Tumour-associated macrophages secrete pleiotrophin to promote PTPRZ1 signalling in glioblastoma stem cells for tumour growth. Nat Commun 2017;8:15080. [PubMed: 28569747]

48. Cloughesy TF, Mochizuki AY, Orpilla JR, Hugo W, Lee AH, Davidson TB, et al. Neoadjuvant anti-PD-1 immunotherapy promotes a survival benefit with intratumoral and systemic immune responses in recurrent glioblastoma. Nat Med 2019;25(3):477–86. [PubMed: 30742122]

Synopsis

Single-cell profiling using mass cytometry and multiplex immunohistochemistry reveals distinct intratumoral immune landscapes in de novo and recurrent glioblastoma, and an increase in activated perivascular T cells at recurrence is shown to associate with improved clinical outcome.

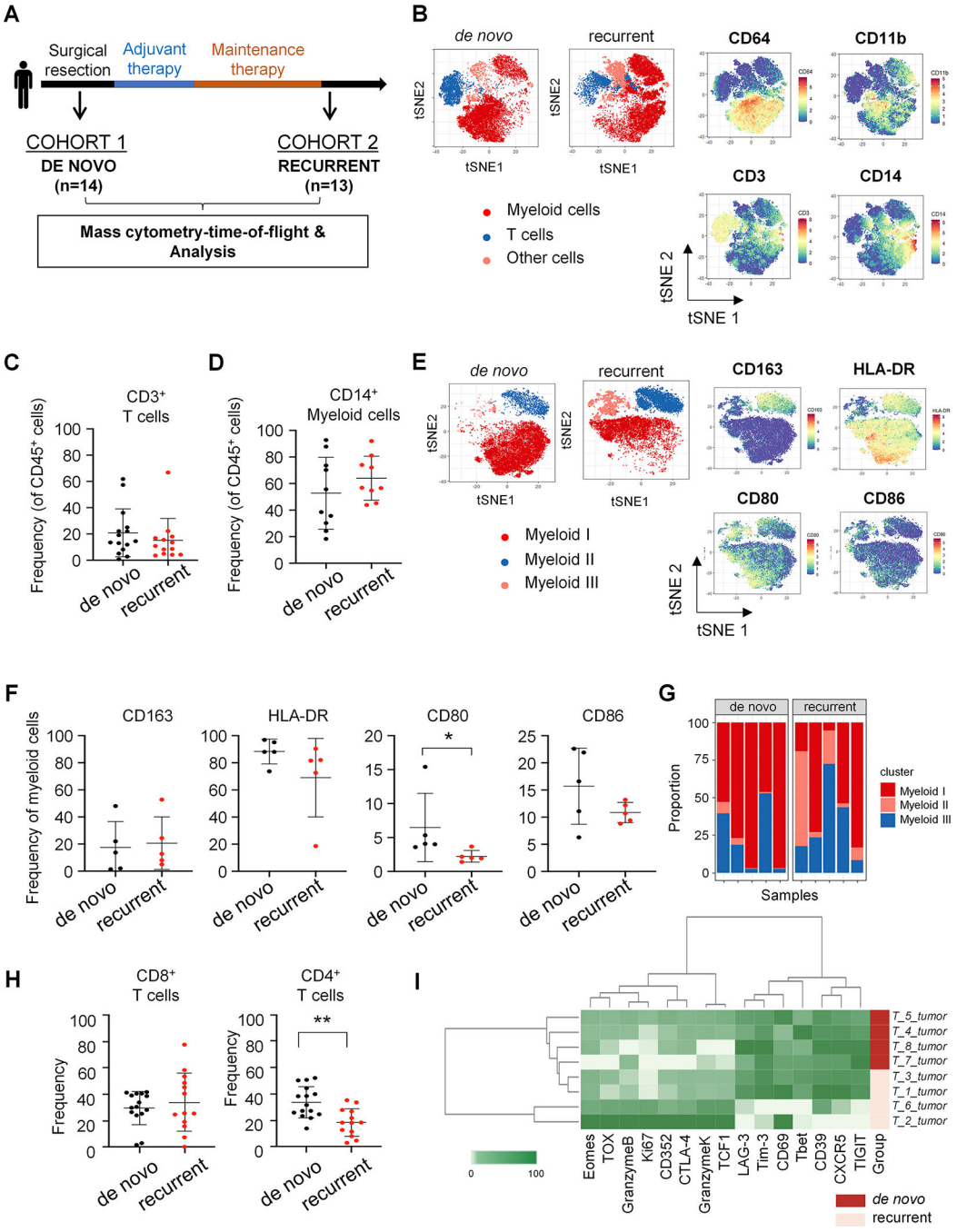

Figure 1. Immune composition of *de novo* and rGBM

A. Schematic of the patient cohorts included in the CyTOF analysis. **B.** CyTOF t-SNE plots of $CD45^+$ infiltrating cells in *de novo* and recurrent tumors assessed together in one experiment using FlowSOM analysis. Left, t-SNE plot shows overlay of myeloid cells (red, defined as $CD14^+CD64^+CD15^+$), T cells (blue, defined as $CD3^+$) and other cells (pink). Right, color gradient plots show expression of CD64, CD11b, CD3 and CD14. **C.** Percentage of $CD3^+$ T cells detected in *de novo* and rGBM tumors. **D.** Percentage of $CD14^+$ myeloid cells detected in *de novo* and recurrent GBM tumors. **E.** CyTOF t-SNE plots of

de novo and recurrent tumors from one experiment using FlowSOM analysis. Left, t-SNE plot gated on $CD45^+$ myeloid cells showing subsets including Myeloid I (red), Myeloid II (blue) and Myeloid III (pink). On the right, color gradient plots show expression of CD163, HLA-DR, CD80 and CD86. **F.** Percentage of all myeloid cells expressing CD163, HLA-DR, CD80, CD86 detected in *de novo* and rGBM tumors. **G.** $CD45^+$ myeloid-cell composition in *de novo* and rGBM tumors. **H.** Percentage of $CD8^+$ (left) and $CD4^+$ (right) T cells detected in *de novo* and rGBM. **I.** Heatmap showing relative expression of phenotypic markers by PD-1^+CD8^+ T cells in *de novo* (red) or rGBM (pink) tumor samples. Statistical significance calculated using two-tailed Mann-Whitney test; shown is mean with error bars indicating SD; *, $P<0.05$; unpaired two-tailed *t*-test.

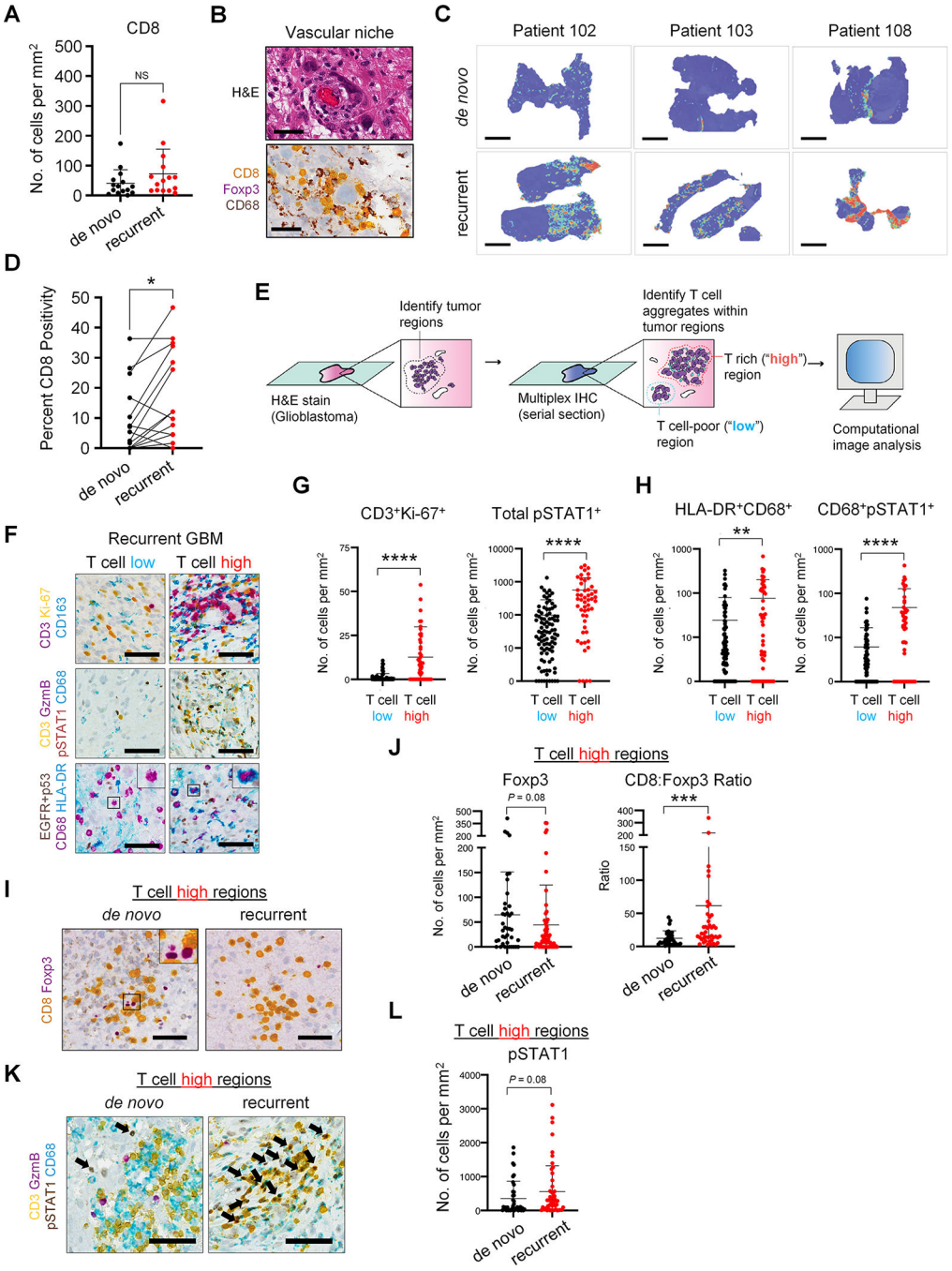

Figure 2. Perivascular T cell–enriched regions differentiate d*e novo* and rGBM.

A. Whole tumor quantification of $CD8^+$ T cells by mIHC in *de novo* and rGBM. **B.** Representative images of the vascular region in GBM stained for hematoxylin- and eosin (top) and CD8, Foxp3 and CD68 (bottom). **C.** Representative heatmaps of CD8 expression in paired *de novo* and recurrent GBM tumors from three patients. **D.** Paired analysis showing percent tumor regions enriched for $CD8^+$ cells among *de novo* and rGBM tumors. **E.** Schematic overview showing image analysis workflow to detect T-cell aggregates within tumor regions. **F.** Representative images showing $CD3^+$ T cells and $CD68^+$ macrophages

detected among T-cell low (left) and T-cell high (right) regions in rGBM. For **G**, **H**, **J**, and **L**, multiple regions defined as T-cell high and T-cell low were identified for each *de novo* and rGBM sample analyzed (Supplemental Table S3). **G.** Quantification of $CD3^+Ki\text{-}67^+$ cells and $pSTAT1^+$ cells in T-cell low and T-cell high regions in rGBM. **H.** Quantification of $HLA\text{-}DR^+CD68^+$ and $CD68^+pSTAT1^+$ myeloid subsets in T-cell low and T-cell high regions in rGBM. **I.** Images showing $CD8^+$ (yellow) and $FOXP3^+$ (purple) cells detected in T-cell high regions in *de novo* (left) and recurrent (right) GBM. **J.** Quantification of $FOXP3^+$ cells (left) and ratio of $CD8^+$ to $FOXP3^+$ cells in T-cell high regions of *de novo* and rGBM. **K.** Images showing $CD3^+$ (yellow), $GzmB^+$ (purple), $pSTAT1^+$ (brown), and $CD68^+$ (teal) cells in T-cell high regions of *de novo* and rGBM tumors. **L.** Quantification of total pSTAT1 expression in T-cell high regions in *de novo* and rGBM tumors. Scale bars, 60 mm. *, $P<0.05$; **, $P<0.01$; ***, $P<0.001$; ****, $P<0.0001$; error bars indicate SD; statistical significance calculated using two-tailed Mann-Whitney test (A, F, G, I, K) or paired Wilcoxon test (C).

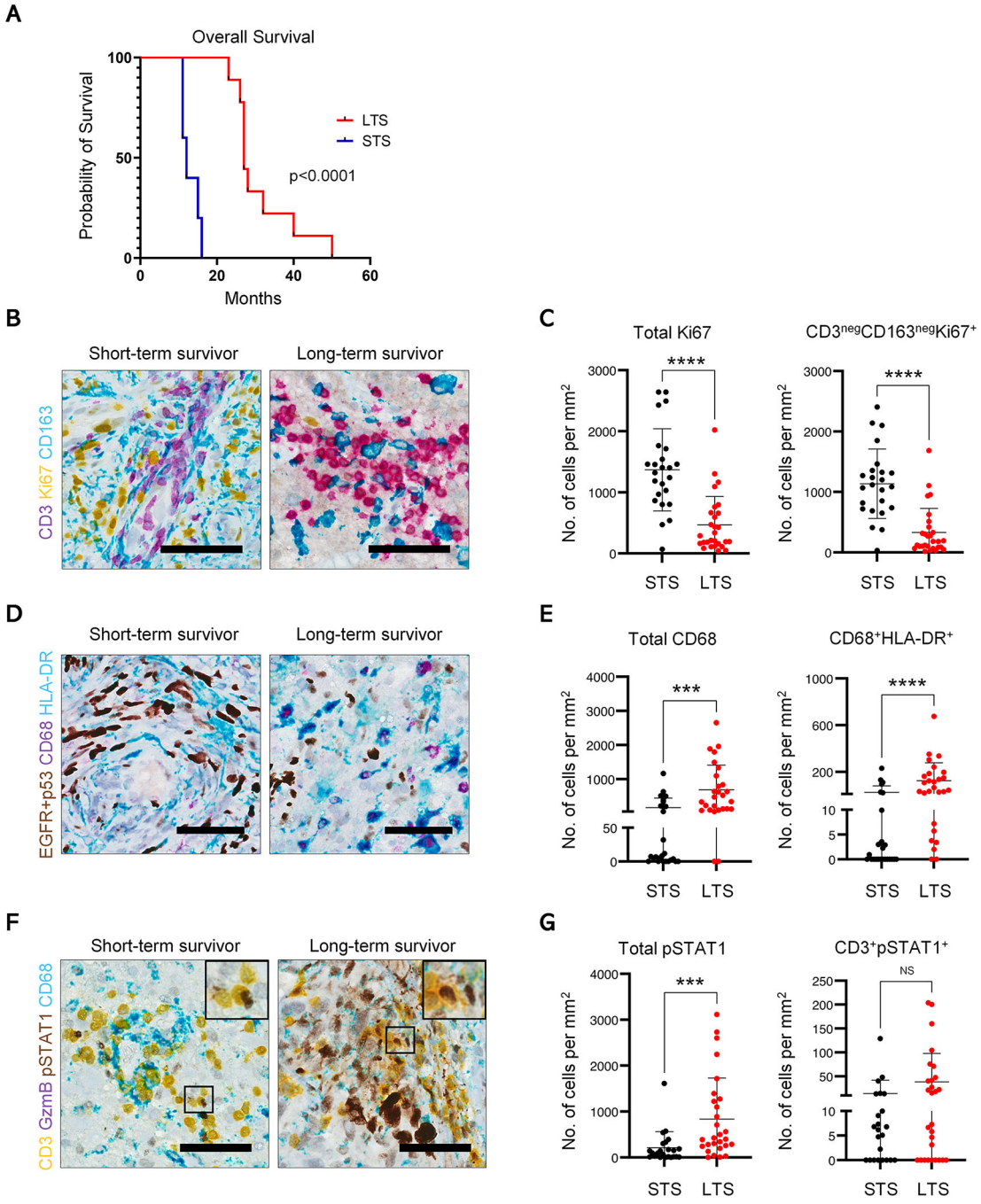

Figure 3. Immune contexture of T-cell high tumor regions in rGBM associates with patient outcomes.

A. Kaplan-Meier plot of overall survival for short-term survivors (STS, N=7) and long-term survivors (LTS, N=9) with GBM. Cohorts were determined by k-means clustering and the median overall survival of the STS group was 11.5 months compared to 27.5 months in the LTS group (P<0.0001). **B.** Representative images showing CD3 (purple), Ki-67 (yellow), and CD163 (teal) expression in T-cell high regions in rGBM tumors for the STS and LTS cohorts. **C.** Quantification of total Ki-67^{+} (left) and CD3^{-}CD163^{-}Ki-67^{+} (right)

expression in T-cell high regions for the STS and LTS cohorts. **D.** Representative images of EGFR+p53 (brown), CD68 (purple), HLA-DR (teal) expression in T-cell high regions in recurrent tumors for the STS and LTS cohorts. **E.** Quantification of $CD68^+$ (left) and $CD68^+HLA\text{-}DR^+$ (right) expression in T-cell high regions of recurrent tumors for the STS and LTS cohorts. **F.** Representative images of CD3 (yellow), GzmB (purple), pSTAT1 (brown), and CD68 (teal) expression in T-cell high regions in rGBM for the STS and LTS cohorts. **G.** Quantification of total $pSTAT1^+$ (left) and $CD3^+pStat1^+$ (right) expression in T-cell high regions in the rGBM for the STS and LTS cohorts. Scale bars, 60 mm. *, $P<0.05$; **, $P<0.01$; ***, $P<0.001$; ****, $P<0.0001$; error bars indicate SD; statistical significance calculated using Log-Rank (Mantel-Cox) test (A) or two-tailed Mann-Whitney test (C, E, G).

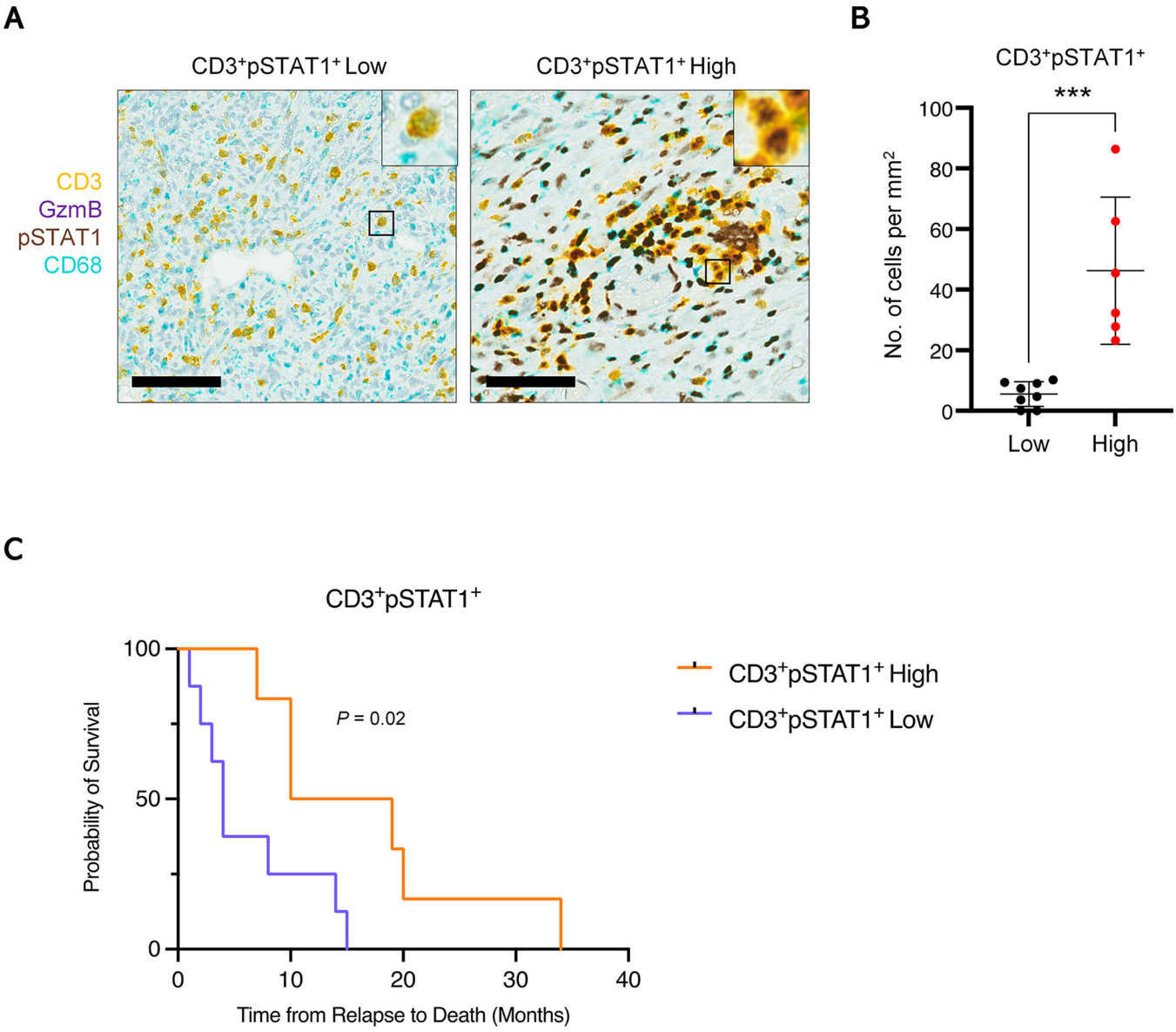

Figure 4. CD3$^+$pSTAT1$^+$ cells associate with increased survival at time of GBM recurrence.

Tumors from patients with rGBM were segregated using maximal selected rank statistics based on CD3$^+$pSTAT1$^+$ and classified as low (<12 cells/mm^2) or high (≥22 cells/mm^2) expression. **A.** Representative images showing CD3 (yellow), GzmB (purple), pSTAT1 (brown), and CD68 (teal) in rGBM tumors classified as low or high CD3$^+$pSTAT1$^+$ expression. Scale bars, 60mm. **B.** Quantification of CD3$^+$pSTAT1$^+$ cells detected in rGBM tumors classified as low or high expression. **C.** Kaplan-Meier plot showing time from recurrence to death for patients with rGBM tumors displaying high or low expression of CD3$^+$pSTAT1$^+$ cells. ***, P<0.001; error bars indicate SD; statistical significance calculated using two-tailed Mann-Whitney test.